

1 | **Reconsidering initial Pb in titanite in the context of *in situ* dating**

2 | **(Revision 1)**

3 |  
4 | Chloë E. Bonamici\*

5 | Tyler B. Blum

6 | Department of Geoscience, University of Wisconsin-Madison, 1215 W. Dayton St., Madison,  
7 | WI 53706

8 |  
9 |  
10 | **Abstract**

11 | *In situ* U-Pb dating of titanite, which can preserve trace-element records of various  
12 | petrologic processes but also incorporates significant initial Pb, has proliferated in recent years.  
13 | The widespread use of titanite data to construct tectonic P-T-t paths warrants careful assessment  
14 | of the available dating techniques, as well as attention to the assumptions that underpin the U-Pb  
15 | data analysis. This contribution provides the first direct comparison of the two major analytical  
16 | methods – SHRIMP (SIMS) and LA-ICP-MS – for *in situ* U-Pb titanite dating. A set of well-  
17 | characterized titanite grains from Harrisville, NY, in the Adirondack Mountains were analyzed  
18 | for U-Th-Pb isotopes along the same cross-grain traverses by SHRIMP and LA-ICP-MS. Both  
19 | LA-ICP-MS and SHRIMP datasets define approximately linear arrays on the Tera-Wasserburg  
20 | Concordia (semi-total Pb/U) diagram and would commonly be interpreted as representing a  
21 | single date population with minor scatter. However, previous studies have suggested that  
22 | Adirondack titanite actually records two regionally well-defined thermal events, ~50-100 m.y.  
23 | apart. When titanite data arrays are treated in detail, attempts to determine concordia-intercept

---

\* Corresponding author. E-mail: [bonamici@wisc.edu](mailto:bonamici@wisc.edu). Phone: +1 608 263 7754.

24 ages by robust three-dimensional linear regression produce large uncertainties and/or poor fit  
25 statistics that suggest that the data are not, in fact, isochronous. Grain-by-grain analysis of U-Pb  
26 titanite data shows that different subsets of titanite (determined by additional geochemical and  
27 microstructural data) show different patterns of U-Pb data. By comparing predictions for Pb-  
28 ingrowth evolution paths in Tera-Wasserburg diagrams with observed data, it is possible to  
29 recognize both a change in initial Pb composition and Pb loss in the Adirondack titanite U-Pb  
30 dataset. This study provides an example of how greater geochronologic detail can be extracted  
31 from large *in situ* U-Pb titanite datasets. Even when precise dates are not recovered, geological  
32 processes and events that cause data scatter can be recognized through analysis of U-Pb data  
33 patterns using the Tera-Wasserburg diagram.

34

35 **Keywords:** titanite; U-Pb geochronology; initial Pb correction; LA-ICP-MS; SHRIMP

36

37

38

39

40

41

42

43

44

45

46

47

48

49  
50  
51  
52  
53  
54  
55  
56  
57  
58  
59  
60  
61  
62  
63  
64  
65  
66  
67  
68  
69  
70  
71

## Introduction

Titanite is an increasingly popular U-Pb geochronometer and petrogenetic indicator in the study of crystalline rocks (e.g., Aleinikoff et al., 2002; 2004; Chen et al., 2016; Essex and Gromet, 2000; Gao et al., 2012; Garber et al., 2017; Holder and Hacker, 2019; Jung and Hellebrand, 2007; Kirkland et al., 2016, 2017; Kohn, 2017; Kohn and Corrie, 2011; Li et al., 2010; Marsh and Smye, 2017; Olierook et al., 2019; Papapavlou et al., 2017, 2018; Scibiorski et al., 2019; Stearns et al., 2015; Storey et al., 2007; Timms et al., 2019). By comparison to zircon, titanite is more reactive and therefore has the potential to display a greater range of petrologic, geochemical, and microstructural variations to inform interpretations of petrogenesis and deformation (Kohn, 2017). The major challenges in applying titanite as a geochronometer are its generally low U and radiogenic Pb concentrations and its tendency to incorporate substantial initial Pb (e.g., Aleinikoff et al., 2002; Frost et al., 2000; Prowatke and Klemme, 2005; Tiepolo et al., 2002).

Initial Pb ( $Pb_i$ ) must be corrected for and therefore complicates accurate U-Pb geochronometry of high- $Pb_i$  phases, like titanite, apatite, allanite, and rutile (e.g., Chew et al., 2014; Kirkland et al., 2017; Rubatto and Scambelluri, 2003; Schoene and Bowring, 2006; Wohlgemuth-Ueberwasser et al., 2017) Here, we use  $Pb_i$  to mean the Pb that is incorporated into a mineral at the time of crystallization or recrystallization, irrespective of its source and isotopic composition.  $Pb_i$  includes what is often called “common Pb”, Pb representing long-term ingrowth from actinides incorporated in the primordial Earth (Stacey and Kramers, 1975).  $Pb_i$  can also include Pb acquired from nearby actinide-partitioning minerals that have ingrown Pb with a non-primordial isotopic composition. The most widely used  $Pb_i$  corrections derive from the models of Stacey and Kramers (1975) and involve assumptions about  $Pb_i$  composition based

72 on the average, reservoir-scale geochemical behavior of Pb – i.e., assumptions about crustal  
73 evolution at the scale of an orogenic region, a crustal domain, or even bulk silicate Earth. For Pb<sub>i</sub>  
74 corrections that employ these models to be accurate, the geochronology sample to which they are  
75 applied must be compositionally representative of the large-scale reference reservoir, a  
76 requirement that is problematic in the context of intragrain U-Pb measurements. Techniques for  
77 *in situ* U-Pb dating, like SIMS/SHRIMP and LA-ICP-MS, complicate Pb<sub>i</sub> corrections because  
78 they sample micron-scale intracrystalline domains (compositional zones), which may now be  
79 chemically and isotopically decoupled from their original environments of formation, including  
80 coexisting phase assemblages and fluids. For instance, even when Pb<sub>i</sub> is measured in a low-U  
81 phase (e.g., K-feldspar) co-located with a zoned geochronometer, it can be difficult to determine  
82 which zone within the geochronometer formed in equilibrium with that phase.

83 A common approach for correcting U-Pb isotope data for Pb<sub>i</sub> is to calculate a Pb<sub>i</sub>  
84 composition based on an estimated age and a crustal evolution model, often the one- or two-stage  
85 model of Stacey and Kramers (1975). The two most common variants of this approach are the  
86 ‘204 method’ and the ‘207 method’. In the 204 method, Pb<sub>i</sub> <sup>204</sup>Pb/<sup>206</sup>Pb is can be calculated  
87 based on a crustal evolution model; measured in a reference material considered representative  
88 of the crustal Pb isotope composition for the sample; or measured in a co-existing low-U phase  
89 within the sample, such as K-feldspar (DeWolf and Mezger 1994; McGregor et al., 2019), and  
90 the total <sup>204</sup>Pb/<sup>206</sup>Pb is measured to determine Pb<sub>i</sub> abundance (e.g., Ireland and Williams, 2003;  
91 Stern, 1997; Storey et al., 2006; Williams, 1998) (Appendix). In the 207 method, Pb<sub>i</sub> <sup>207</sup>Pb/<sup>206</sup>Pb  
92 is based on either a model value or a measured value in a co-existing phase, as well as an  
93 expected age for the titanite (Appendix). The 204 method has traditionally been preferred for  
94 data collected by SIMS/SHRIMP analysis, during which <sup>204</sup>Pb is readily measured (Stern et al.,

95 2009; Stern, 1997; Storey et al., 2006). The 207 method is commonly preferred for data collected  
96 by LA-ICP-MS analysis, during which  $^{204}\text{Hg}$  contaminants in the Ar plasma interfere on mass  
97 204 (Gehrels et al., 2008; Horstwood et al., 2003; Schoene, 2014; Storey et al., 2006), though  
98 recent developments in quadrupole LA-ICP-MS analysis can mitigate this problem. The  
99 underpinning assumption for the 204 and 207 method corrections that rely on model values is  
100 that the continental crust has evolved as a coherent and largely closed reservoir with respect to U  
101 and Pb isotope systematics, and that titanite will crystallize with  $\text{Pb}_i$  composition representative  
102 of this bulk crustal reservoir. The idea of an “average” or “bulk” composition, however, can  
103 break down at the grain scale, where Pb isotope compositions of individual phases depend on  
104 phase-specific U and Pb partitioning. For instance, titanite forming from breakdown of rutile  
105 may partition radiogenic Pb from rutile in addition to average, ambient Pb, and thus have a  
106 different effective  $\text{Pb}_i$  composition from the bulk rock (Marsh and Smye, 2018). Thus, *in situ*  
107 geochronology of phases that incorporate both U and  $\text{Pb}_i$  require careful evaluation of  $\text{Pb}_i$   
108 sources and possible grain-scale U-Pb fractionation.

109 Another approach for titanite U-Pb data correction is equivalent to the classic isochron  
110 regression method and employs the semi-total Pb/U (Tera-Wasserburg) or total Pb/U diagrams  
111 (Ludwig, 1998, 2009, 2012). The samples used to define the linear regression can be  
112 permutations of grain separates or individual grains but can also be multiple (e.g., Amelin, 2009;  
113 Verts et al., 1996), *in situ* intergrain or intragrain analyses (e.g., Holder and Hacker, 2019; Kohn  
114 and Corrie, 2011; Olierook et al., 2018; Storey et al., 2006). In practice, it is common to  
115 constrain the  $\text{Pb}_i$   $^{207}\text{Pb}/^{206}\text{Pb}$  composition based on a Stacey and Kramers (1975) model and force  
116 the regression through this  $\text{Pb}_i$  composition (e.g., Kohn and Corrie, 2011). However, it is  
117 becoming more common to treat  $\text{Pb}_i$  composition as a variable that is retrieved from the

118 regression process (e.g., Kirkland et al., 2017). The Tera-Wasserburg-based isochron regression  
119 correction method can avoid the pitfalls of assuming a crustal Pb isotope composition but only  
120 works if i) the  $Pb_i$  composition is uniform in the grains or domains used to determine the  
121 isochron ii) measured grains/domains formed at the same time (are isochronous), and iii) in the  
122 case that the  $Pb_i$  composition is not fixed a priori, a sufficiently large range of intracrystalline  
123 U/Pb and Pb/Pb ratios are sampled to tightly constrain the regression. With recent detailed  
124 characterizations of titanite (e.g., Essex and Gromet, 2000; Bonamici et al., 2015; Garber et al.,  
125 2017; Marsh and Smye, 2017; Olierook et al., 2018), it is clear that  $Pb_i$  can and does vary over  
126 timescales of titanite growth and/or recrystallization, undercutting the first requirement for the  
127 isochron regression approach in some cases.

128 U-Pb isotope data for  $Pb_i$ -rich phases are treated on the Tera-Wasserburg Concordia  
129 diagram in order to explicitly show the  $Pb_i$  contribution to U-Pb isotope composition. The Tera-  
130 Wasserburg diagram is a two-dimensional projection of the total Pb/U isochron diagram (Ludwig,  
131 1998), which allows for direct display of the  $Pb_i$  trends in a dataset. The familiar Wetherill  
132 concordia diagram works well for low- $Pb_i$  phases and excels at revealing open system behavior  
133 that affects the radiogenic U/Pb ratio (e.g., Schoene, 2014). In contrast, the U-Pb data patterns on  
134 the Tera-Wasserburg diagram reflect a combination of  $Pb_i$ -radiogenic Pb mixing and open  
135 system behavior. Such patterns can, consequently, be less straightforward to interpret.

136 This work applies different  $Pb_i$  correction methods to a suite of well-characterized  
137 Grenville-aged titanite grains from the Adirondack Mountains of New York. A review of U-Pb  
138 isotope evolution in the semi-total Pb/U isochron (Tera-Wasserburg) diagram illustrates how  
139 both intragrain  $Pb_i$  compositional variations and grain scale Pb loss can be preserved within *in*  
140 *situ* data sets. This analytical framework is applied to two U-Pb datasets for the same titanite

141 grains – one collected by SHRIMP and the other collected by LA-ICP-MS. Comparison of the  
142 two in situ analytical techniques allows recognition of non-isochronous data and highlights the  
143 relative strengths of each technique. These results reinforce both the complexity and  
144 opportunities in microanalysis of geochronometers with significant initial Pb.

145

146

### **Samples and Methods**

147 Titanite-bearing samples used in this study are high-grade, midcrustal tectonites from the  
148 Adirondack region of upstate New York. Titanite grains are hosted in metasyenite collected  
149 within the Carthage-Colton mylonite zone, a major structure developed at the boundary between  
150 Grenville-aged crustal domains. The Adirondack Lowlands to the northwest of the CCMZ record  
151 peak metamorphic conditions during the Shawinigan-AMCG phase of the Grenville orogeny at  
152 ca. 1150 Ma, whereas the Adirondack Highlands to the east-southeast of the CCMZ record peak  
153 metamorphic conditions during the Ottawa phase at ca. 1050 Ma (Mezger et al., 1993; 1991a;  
154 1991b). The tectonic context of the CCMZ has been previously discussed by Mezger et al.  
155 (1991a), Mezger et al. (1991b), Mezger et al. (1992), Mezger et al. (1993), Cartwright et al.  
156 (1993), Streepey et al. (2001), Baird and MacDonald (2004), Johnson et al. (2004), Johnson and  
157 Selleck (2005), McLelland et al. (2010), and Bonamici et al. (2014). Structural, petrologic, and  
158 geochemical characteristics of the specific Harrisville location of samples for the current study  
159 have been addressed by Lamb (1993), Cartwright et al. (1993), Baird and MacDonald (2004),  
160 Heumann (2004), Johnson and Selleck (2005), Bonamici et al. (2014), and Bonamici et al.  
161 (2015).

162 Regional geochronology provides constraints within which to study and interpret U-Pb  
163 titanite data from the CCMZ. Bonamici et al. (2015) documented the intragrain zoning patterns

164 of SHRIMP U-Pb dates within six Harrisville titanite samples (Table 1). Four different  
165 generations of titanite were distinguished on the basis of microstructure and reinforced on the  
166 basis of chemistry and oxygen-isotope zoning patterns (Bonamici et al., 2014, 2015). These  
167 generations are interpreted to be igneous titanite crystallized in the protolith syenite at ~1160 Ma  
168 (Type-1); igneous grains variably reset during later granulite-facies metamorphism at ca. 1050  
169 Ma (Type-2); titanite from veins that likely intruded at ca. 1050 Ma (Type-3); and igneous  
170 titanite with metamorphic overgrowths (Type-4). Table 1 provides grain descriptions and further  
171 information summarizing these interpretations. LA-ICP-MS data presented in this study  
172 significantly expand the number of Harrisville titanite grains investigated for U-Pb zoning. U-Pb  
173 ratios were measured in a total of fourteen titanite grains, including one Type-1 grain, five Type-  
174 2 grains, six Type-3, and two Type-4 grains.

175 Titanite was analyzed in thin sections of metasyenite cut into one-inch rounds. Thus, all  
176 analyzed titanite grains are *in situ* with respect to their host microstructures and phase  
177 assemblages. Grains of U-Pb titanite reference material BLR-1 (accepted  $^{206}\text{Pb}/^{238}\text{U}$  age  $1047 \pm$   
178  $0.4$  Ma, Aleinikoff et al., 2007) were embedded in every sample each mount. BLR-1 was used  
179 for calibration under the designation BLS at the Arizona Laserchron Center, along with  
180 secondary reference material Ecstall West zircon (accepted  $^{206}\text{Pb}/^{238}\text{U}$  age  $91.5 \pm 1$  Ma, Butler et  
181 al., 2002), also embedded in each analysis mount. Weighted average ages showing the  
182 performance of the reference material grains in each mount during LA-ICP-MS analysis are  
183 compiled in the Supplementary Materials. Within  $2\sigma$  analytical uncertainties, the dates  
184 determined for these reference materials during SHRIMP and LA-ICP-MS analysis overlap the  
185 accepted ages.



186 SIMS U-Pb dates were collected with the SHRIMP II instrument at the Research School  
187 of Earth Sciences (RSES) at the Australian National University using a focused, 4.5-nA O<sub>2</sub><sup>-</sup>  
188 primary beam. Data were acquired in single-collector mode with seven successive scans through  
189 species <sup>200</sup>CaTi<sub>2</sub>O<sub>4</sub>, <sup>204</sup>Pb, <sup>206</sup>Pb, <sup>207</sup>Pb, <sup>208</sup>Pb, <sup>238</sup>U, <sup>248</sup>ThO, and <sup>254</sup>UO, with each individual  
190 analysis taking 20 minutes. SHRIMP analysis sputtered pits 35-40 μm in diameter and 2-3 μm  
191 deep (Fig. 1A). Grains of U-Pb titanite standard BLR-1 were analyzed at regular bracketing  
192 intervals throughout each analysis session. Total <sup>238</sup>U/<sup>206</sup>Pb, <sup>207</sup>Pb/<sup>206</sup>Pb, and <sup>204</sup>Pb/<sup>206</sup>Pb ratios  
193 reported in Table S1 are corrected for U/Pb instrumental fractionation but are not corrected for  
194 Pb<sub>i</sub>. SHRIMP radiogenic ratios and <sup>206</sup>Pb/<sup>238</sup>U dates were initially reported in Bonamici et al  
195 (2015), where they were corrected for Pb<sub>i</sub> with the 204 method using <sup>204</sup>Pb/<sup>206</sup>Pb measured on  
196 long-term RSES lab reference material, Broken Hills feldspar (<sup>206</sup>Pb/<sup>204</sup>Pb = 16.00, <sup>207</sup>Pb/<sup>204</sup>Pb =  
197 15.39, and <sup>208</sup>Pb/<sup>204</sup>Pb = 35.66; Gulson, 1984). For the current study, SHRIMP data have been  
198 re-corrected (Table S1) with the 204 method using both (1) the Stacey and Kramers (1975)  
199 model and (2) the K-feldspar Pb-Pb ratios reported by Mezger et al. (1992) for a shear zone in  
200 the Diana metasyentite (sample 90-49: <sup>206</sup>Pb/<sup>204</sup>Pb = 17.132, <sup>207</sup>Pb/<sup>204</sup>Pb = 15.427, and  
201 <sup>208</sup>Pb/<sup>204</sup>Pb = 36.461). The dates corrected with Mezger et al. (1992) are preferred because these  
202 Pb values come from the same outcrops as the titanite samples used in the current study. To  
203 facilitate comparison with LA-ICP-MS data, the SHRIMP data have also been corrected with the  
204 207 method (Table S1) using the Stacey and Kramers (1975) Pb isotope model implemented  
205 through the Arizona Laserchron Center spreadsheet software, “Titanite AgeCalc 207Pbc”.

206 Prior to LA-ICP-MS analysis, SHRIMP pits and carbon coats were removed from  
207 samples by repolishing with 1-μm diamond-grit suspension. Samples were cleaned with several  
208 cycles of sonication in distilled water and ethanol. LA-ICP-MS U-Pb dates were collected on a

209 Nu HR ICP-MS coupled to a Photon Machines Analyte G2 Excimer laser at the Arizona  
210 Laserchron Center at the University of Arizona. Data were acquired in static multicollector mode,  
211 with  $^{202}\text{Hg}$  and  $^{204}\text{Pb}$  collected on ion counters and  $^{206}\text{Pb}$ ,  $^{207}\text{Pb}$ ,  $^{208}\text{Pb}$ ,  $^{238}\text{U}$ , and  $^{232}\text{Th}$  collected  
212 on  $10^{11}$ -ohm resistor Faraday cups. Each analysis included 15 seconds of background counting,  
213 15 one-second laser pulses for sample signal and 30 seconds of wash-out time for a total of  
214 approximately 60 seconds per analysis. Laser ablation produced pits 35-40  $\mu\text{m}$  in diameter and  
215  $\sim 15$   $\mu\text{m}$  deep (Fig. 1B). Grains of U-Pb titanite standard BLR-1 ( $^{206}\text{Pb}/^{238}\text{U}$  age 1047 Ma,  
216 Aleinikoff et al., 2007; also called BLS in the Laserchron lab) were analyzed at regular  
217 bracketing intervals throughout each analysis session. Total  $^{238}\text{U}/^{206}\text{Pb}$ ,  $^{207}\text{Pb}/^{206}\text{Pb}$ , and  
218  $^{204}\text{Pb}/^{206}\text{Pb}$  ratios reported in Table S2 were corrected for U/Pb instrumental fractionation, as  
219 well as the  $^{204}\text{Hg}$  interference on  $^{204}\text{Pb}$ . The  $^{204}\text{Pb}$  interference correction is accomplished by  
220 subtraction of mass 204 counts that are inferred to come from  $^{204}\text{Hg}$  based on the measurement  
221 of mass 202 and an assumed natural  $^{202}\text{Hg}/^{204}\text{Hg}$  ratio of 4.34 (Gehrels et al. 2008). Data in  
222 Table S2 and Figures 2, 3, 4, and 6 are not corrected for  $\text{Pb}_i$ . Radiogenic ratios and  $^{206}\text{Pb}/^{238}\text{U}$   
223 dates reported for LA-ICP-MS data (Table S2) were corrected for  $\text{Pb}_i$  by an iterative 207 method  
224 implemented using internal Arizona Laserchron Center spreadsheet-based software (“Titanite  
225 AgeCalc 207Pbc”). This correction uses the raw  $^{206}\text{Pb}/^{238}\text{U}$  ratio before  $\text{Pb}_i$  correction as an  
226 initial estimate of expected age and the Stacey and Kramers (1975) model for an estimate of the  
227  $\text{Pb}_i$  composition (Appendix). The 207-corrected age then recalculated several more times with  
228 the 207-corrected age from the previous iteration used as the expected age for each subsequent  
229 iteration. For titanite U-Pb measurements in this study, the calculation rapidly converges to a  
230 stable corrected age within  $\leq 5$  iterations. To facilitate comparison with the SHRIMP data, the

231 LA-ICP-MS data have also been corrected with the 204 method (Table S2) using the Stacey and  
232 Kramers (1975) model.

233 Data are compared using total isotope ratios, uncorrected for Pb<sub>i</sub>, on Tera-Wasserburg  
234 Concordia plots. Error ellipses in Figures 2, 3 and 9 represent 2σ analytical uncertainties,  
235 including counting statistics and U/Pb instrumental fractionation (as calibrated with titanite  
236 BLR/BLS reference material). Uncertainties on <sup>204</sup>Pb/<sup>206</sup>Pb for SHRIMP data have been  
237 conservatively estimated at 3% (1σ), which is double the largest <sup>207</sup>Pb/<sup>206</sup>Pb uncertainty reported  
238 for SHRIMP data. Uncertainties on all other ratios are as reported by the respective lab (Tables  
239 S1 and S2). Error correlations between <sup>238</sup>U/<sup>206</sup>Pb, <sup>207</sup>Pb/<sup>206</sup>Pb, and <sup>204</sup>Pb/<sup>206</sup>Pb ratios are  
240 considered to be small and are neglected for the sake of more direct comparison of data arrays.

241 Two- and three-dimensional linear regressions were implemented in Isoplot 3.75 using  
242 Model 1, which weights each measurement by the inverse square of the analytical errors under  
243 the assumption that analytical errors are the only source of uncertainty in the data (Ludwig,  
244 2012). A Model 1 regression fit is considered reasonable if the probability of fit is ≥ 0.05.  
245 Probability of fit for each regression is used as an indicator of additional (geological) sources of  
246 scatter. Other models for regression (Models 2 and 3) were not considered to avoid additional  
247 assumptions about sources of uncertainty (beyond analytical).

248

249

## Results

250 When considered in aggregate, LA-ICP-MS and SHRIMP datasets for Harrisville titanite  
251 grains define steep, approximately linear trends on Tera-Wasserburg or semi-total Pb/U diagrams  
252 (Fig. 2). The LA-ICP-MS data array spread is larger for two reasons: 1) more than twice as many  
253 titanite grains were analyzed by LA-ICP-MS as by SHRIMP (Fig. 3) and many of the grains

254 analyzed by laser had lower  $Pb_i$  that extends the array farther toward concordia; and 2) the large  
255  $^{207}Pb/^{206}Pb$  uncertainties on the LA-ICP-MS data for the highest- $Pb_i$  grains appear to stretch the  
256 laser data array vertically. However, close comparison of the grains analyzed by both LA-ICP-  
257 MS and SHRIMP in Figure 3, shows that, regardless of error ellipse shape, the individual data  
258 points are centered at nearly identical locations.

259 Tera-Wasserburg-based, two-dimensional regression of the aggregate SHRIMP dataset  
260 yields a concordia intercept age of  $1138 \pm 19$  Ma with  $MSWD = 4.4$ , whereas 2D regression of  
261 the aggregate LA-ICP-MS dataset yields a concordia intercept age of  $1067 \pm 12$  Ma with  $MSWD$   
262  $= 2.0$  (Table S3). We note that the regression of SHRIMP data yield a  $MSWD$  indicating well  
263 scatter beyond that expected based on analytical uncertainty alone, whereas that the precision of  
264 LA-ICP-MS data result in a more ambiguous  $MSWD$  value. No concordia-intercept ages can be  
265 obtained for either aggregate dataset (LA-ICP-MS or SHRIMP) using a total Pb/U isochron  
266 (linear 3D) regression that includes the  $^{204}Pb/^{206}Pb$  ratio (Table 1).

267 For Harrisville titanite samples, greater  $^{238}U/^{206}Pb$  (average 2.3%  $1\sigma$ ) than  $^{207}Pb/^{206}Pb$   
268 analytical uncertainties (average 1.0%  $1\sigma$ ) suggest that the U/Pb calibration dominates overall  
269 SHRIMP analytical uncertainties. In contrast, greater  $^{207}Pb/^{206}Pb$  (average 5.1%  $1\sigma$ ) than  
270  $^{238}U/^{206}Pb$  (average 2.6%  $1\sigma$ ) analytical uncertainties indicate that abundance sensitivity  
271 dominates overall LA-ICP-MS analytical uncertainties.

272 On a grain-by-grain basis, both SHRIMP and LA-ICP-MS U-Pb measurements show a  
273 range of behavior, with several grains having tightly clustered data (i.e. showing limited  
274  $^{238}U/^{206}Pb$  or  $^{207}Pb/^{206}Pb$  dispersion) (Fig. 3). For those grains with tightly clustered spot analyses,  
275 both 2D and 3D regressions of the U-Pb measurements yield large concordia-intercept age  
276 uncertainties ( $> \pm 50$  Ma), as well as large  $MSWD$  values for SHRIMP data sets. Titanite grains

277 from sample HA13 are an exception, showing sufficient analysis dispersion to provide  
278 moderately tight constraints on concordia-intercept ages regressed from LA-ICP-MS data (Fig.  
279 3). SHRIMP U-Pb measurements for the HA13 S2 grain show a similar dispersion to LA-ICP-  
280 MS measurements and similar concordia-intercept age but with high MSWD values.

281 Results from 3D linear isochron regressions for each titanite Type are described below  
282 with respect to the concordia-intercept age and the regressed  $Pb_i^{207}Pb/^{206}Pb$  value (Table 1, Fig.  
283 4). Several unconstrained 3D regressions produce negative  $^{207}Pb/^{206}Pb$  (y-axis) intercept values  
284 because tightly clustered data do not adequately constrain the linear regression toward the  
285 common Pb plane, resulting in a very large range of possible intercept values with a negative  
286 mean. Several constrained 3D regressions produce undefined  $^{207}Pb/^{206}Pb$  values because very  
287 large uncertainties push the mean regressed  $^{206}Pb/^{204}Pb$  value to zero (Table 1), the lowest  
288 allowed  $^{206}Pb/^{204}Pb$  value for a constrained regression solution. Table S3 shows 2D regression  
289 results, but these are not discussed in the text in order to avoid redundancy and because the larger  
290 uncertainties on the 2D regression results generally hide details within the datasets.

### 291 **Type 1 titanite results**

292 Constrained 3D linear concordia intercept dates for the Type-1 grain for both LA-ICP-  
293 MS and SHRIMP data are  $> 1200$  Ma, with large uncertainties of  $> 200$  m.y. (Table 1). The  
294 unconstrained regression of LA-ICP-MS data intercepts concordia within analytical uncertainties,  
295 but the unconstrained regression of more precise SHRIMP data set does not (Fig 4B). The Type-  
296 1 titanite grain has both the highest and largest range of  $^{204}Pb/^{206}Pb$  ratios (Tables S1 and S2).  
297 The Type-1 grain also has the lowest overall U, Th, and Pb concentrations. LA-ICP-MS data  
298 points from this low-Pb grain all overlap significantly within error and no interpretable  
299  $^{207}Pb/^{206}Pb$  intercept is obtained with either constrained or unconstrained 3D regressions (Table

300 1). An unconstrained regression of the more precise SHRIMP data yields an upper intercept  
301  $^{207}\text{Pb}/^{206}\text{Pb}$  value of 0.967, similar to the Stacy and Kramers common Pb value of 0.922, though  
302 with large uncertainties (Table 1).

### 303 **Type 2 titanite results**

304 Type-2 titanite grains yield tightly clustered U-Pb data points, both within individual  
305 grains (Fig. 3) and between grains (Fig. 2). Constrained 3D linear regressions of LA-ICP-MS  
306 data return concordia-intercept ages of 1143-1111 Ma, whereas regressions of SHRIMP data  
307 return consistently older concordia-intercept ages of 1182-1146 Ma (Table 1). Both methods  
308 produce intercept-age uncertainties of 48-130 m.y., and the SHRIMP data regressions are also  
309 associated with large MSWD values. Both constrained and unconstrained regressions yield  
310 largely uninterpretable  $^{207}\text{Pb}/^{206}\text{Pb}$  upper intercept values (Table 1), with the possible exception  
311 of grain HA09A S15, which gives values consistent with a mixture of primordial (Stacey and  
312 Kramers common Pb) and radiogenic  $\text{Pb}_i$ .

### 313 **Type 3 titanite results**

314 Aggregated Type-3 data show greater dispersion than Type-2 data, but data for individual  
315 Type-3 grains are more clustered than the aggregate dataset (Fig. 3). Constrained 3D isochron  
316 regressions of LA-ICP-MS Type-3 data yield the youngest concordia intercept ages, ranging  
317 from 935 Ma to 1101 Ma (Table 1, Fig. 4). Some of the older LA-ICP-MS dates have moderate  
318 analytical uncertainties of 28-38 m.y., but many LA-ICP-MS dates are associated with large  
319 analytical uncertainties of 63-190 m.y.. Constrained 3D regression for the one SHRIMP-  
320 analyzed Type-3 grain produces an imprecise concordia intercept age of  $1220 \pm 370$  Ma.  
321 Constrained and unconstrained regressions for most LA-ICP-MS-analyzed grains produce  
322  $^{207}\text{Pb}/^{206}\text{Pb}$  upper intercepts intermediate between the expected radiogenic value ( $\sim 0.08$ ) and the

323 expected Stacey and Kramers common-Pb model value ( $\sim 0.92$ ), though often with very large  
324 uncertainties.

#### 325 **Type 4 titanite results**

326 Data from the Type-4 grains, in aggregate and individually, define approximately linear  
327 or apparently offset linear trends. Whereas overlap in LA-ICP-MS data for grain HA13A-S1  
328 obscures distinct internal data populations, three data populations can be distinguished in both  
329 the LA-ICP-MS and SHRIMP data for HA13A-S2 (Fig. 3). Constrained and unconstrained  
330 regressions of both LA-ICP-MS and SHRIMP data produce very similar Tera-Wasserburg plane  
331 intercepts and concordia intercept ages at 1124-1128 Ma (Table 1, Fig. 4). Uncertainties on LA-  
332 ICP-MS data are  $\sim 25$  m.y. and those for the SHRIMP data are three times larger at 75 m.y.. In  
333 addition, the MSWD value for the regression of the SHRIMP data is much larger than the  
334 MSWD value for LA-ICP-MS data. Most constrained and unconstrained regressions for both  
335 analytical techniques produce  $^{207}\text{Pb}/^{206}\text{Pb}$  upper intercepts intermediate between the expected  
336 radiogenic value ( $\sim 0.08$ ) and the expected Stacy and Kramers common Pb model value ( $\sim 0.92$ ).  
337 The constrained regression for the SHRIMP-analyzed grain produces a  $^{207}\text{Pb}/^{206}\text{Pb}$  upper  
338 intercept greater than the expected Stacy and Kramers common Pb model value, though with  
339 large uncertainties.

#### 340 **Zoning trends within titanite grains**

341 *In situ* U-Pb data can also be assessed in the context of their spatial distribution within  
342 titanite grains (Fig 5; Supplemental Figures; Bonamici et al., 2015). The lower precision of LA-  
343 ICP-MS measurements precludes definitive recognition of intragrain zoning as the oldest and  
344 youngest  $\text{Pb}_i$ -correct dates determined for any given grain overlap within  $2\sigma$  uncertainties;  
345 however, similarity of intragrain trends in grains for which both more precise SHRIMP data and

346 LA-ICP-MS data exist (Fig. 5), suggests that the LA-ICP-MS data are indicative of zoning.  
347 Generally, both LA-ICP-MS and SHRIMP yield older  $^{206}\text{Pb}/^{238}\text{U}$  dates toward grain centers and  
348 younger dates near grain edges (Fig 5; Supplemental Figures); however, there is considerable  
349 intragrain variability in  $\text{Pb}_i$ -corrected dates (particularly for SHRIMP data), which range from  
350 pre-Shawinigan (>1180 Ma) to post-Ottawan (975 Ma). This result is the same, whether the  $\text{Pb}_i$   
351 model is the traditional Stacey and Kramers (1975), the ANU lab Broken Hill feldspar, or the  
352 Mezger et al. (1992), providing that the same  $\text{Pb}_i$  composition is used for all corrections (Table  
353 S1). For a given grain, most  $\text{Pb}_i$ -corrected dates differ significantly from the mean constrained  
354 concordia-intercept date (Fig 5; Supplemental Figures); however, almost all dates overlap within  
355 large uncertainties associated with both the individual  $\text{Pb}_i$  date corrections and the isochron  
356 regressions.

357

## 358 Discussion

### 359 Comparison of LA-ICP-MS and SHRIMP analysis of titanite

360 The collection and comparison of parallel U-Pb data sets for Harrisville titanite allows us  
361 to examine the tradeoffs in analytical precision and data collection rates between the two  
362 techniques for these grains. In general, both techniques recover very similar ranges in isotope  
363 ratios, but the higher analytical precision of the SHRIMP data resolves intragrain complexity that  
364 is obscured by the lower analytical precision of the LA-ICP-MS data. Consequently, the  
365 precision of dates determined through individual  $\text{Pb}_i$  correction is generally lower for LA-ICP-  
366 MS than for SHRIMP (Fig. 5; Tables S1 and S2), reflecting larger uncertainties in the Pb isotope  
367 measurements by LA-ICP-MS and their propagation through the 207-method correction. On the  
368 other hand, the precision of concordia intercepts is generally poorer for SHRIMP than for LA-



369 ICP-MS (Fig. 4), reflecting greater resolvable geologic scatter in the more precise SHRIMP data  
370 and thus poorer fits for linear regressions.

371 *In situ* U-Pb data collected within titanite grains are commonly assumed to represent  
372 single age and Pb<sub>i</sub> populations and are treated as such through the isochron regression method.  
373 The facts that the aggregated Harrisville data (1) cannot be fit with a 3D regression and (2) yield  
374 dates ~70 m.y. apart for 2D regressions (Table 2) point toward significant grain-to-grain age  
375 and/or Pb<sub>i</sub> heterogeneity. Dates determined by the isochron regression method for within-grain  
376 U-Pb data generally overlap the time period spanning the two known orogenic events in the  
377 Adirondack Mountains, from beginning of the AMCG-Shawinigan phase at ca. 1180 Ma through  
378 the end of the Ottawa phase at ca. 1010 Ma (Fig. 4). The poor precision on these regression  
379 dates, however, rarely allows a given date to be clearly assigned to one orogenic phase or the  
380 other, let alone to a restricted period within one of the orogenic phases (Figs. 3, 4). The spread of  
381 regression-determined dates is consistent with the conclusion from previous work that the  
382 Harrisville titanite grains record both the AMCG-Shawinigan and Ottawa events (Bonamici et  
383 al., 2015). It also suggests that regressions are not true isochrons, but rather that they are fits to  
384 mixed, non-isochronous data that are variably resolved with different *in situ* measurement  
385 techniques (see below for further discussion). Larger analytical uncertainties for LA-ICP-MS  
386 data, especially, mask the probable geologic scatter within the data, producing isochron  
387 regressions with MSWD values  $\leq 1$  and probabilities of fit  $> 0.05$ . Only relatively large  
388 propagated uncertainties, typically  $\geq \pm 50$  m.y., suggest the presence of geologic scatter within  
389 the LA-ICP-MS datasets. By comparison, geologic scatter is more apparent in regressions of  
390 SHRIMP data for the same titanite grains, which produce large MSWD values, probabilities of  
391 fit close to zero, and large propagated uncertainties (Fig. 3).

392 Regression-determined dates and  $Pb_i$ -corrected dates for a given grain can be compared  
393 to check for internal consistency between the analytical and correction methods. An ideal titanite  
394 grain that has crystallized at a single time, though with a range of  $Pb_i$  concentrations, should  
395 produce  $Pb_i$ -corrected dates that are identical to one another and to the regressed concordia-  
396 intercept date. Differences in  $Pb_i$ -corrected dates and/or discrepancy between  $Pb_i$ -corrected and  
397 regression-determined concordia-intercept dates would suggest internal zoning and non-  
398 isochronous grain crystallization.  $Pb_i$ -corrected dates are, in fact, not identical across Adirondack  
399 titanite grains. Intragrain zoning of  $Pb_i$ -corrected dates is statistically resolvable along most  
400 traverses measured by SHRIMP, though not by LA-ICP-MS (Fig. 5); nonetheless, the similarity  
401 between several SHRIMP and LA-ICP-MS profile shapes suggests that LA-ICP-MS is detecting  
402 similar isotopic variability. Similarly,  $Pb_i$ -corrected dates and regressed concordia-intercept dates  
403 for a given grain generally overlap within the propagated uncertainties of the respective  
404 correction methods (Fig. 5). However, the resolvable intragrain zoning of  $Pb_i$ -corrected SHRIMP  
405 dates and the poor fit metrics for many of the concordia-intercept regressions suggest that this  
406 overlap is an artefact of temporally close events ( $\leq 100$  m.y. apart at greater than 1 Ga) and  
407 relatively large analytical uncertainties on the *in situ* data.

408 The LA-ICP-MS and SHRIMP datasets for several Adirondack titanite grains also allow  
409 for assessment of differential Pb isotope sensitivity and its potential effects on the accuracy of  
410  $Pb_i$ -corrected dates. Specifically, differential sensitivity to higher-abundance  $^{206}Pb$  relative to  
411 lower-abundance  $^{204}Pb$  or  $^{207}Pb$  could skew measured Pb/Pb ratios used for  $Pb_i$  corrections. A  
412 quick check for differential Pb isotope sensitivity is to compare 204-corrected versus 207-  
413 corrected dates for both the SHRIMP and LAICPMS datasets. SHRIMP data corrected with the  
414 204 and 207 methods yield dates that are essentially identical (Table S1), suggesting that

415 SHRIMP Pb/Pb ratios are not skewed by differential Pb isotope sensitivity. LA-ICP-MS data  
416 corrected by the 204 and 207 methods yield different dates, with those corrected by the 204  
417 method always systematically younger (Table S2). Differences between the LA-ICP-MS and  
418 SHRIMP datasets can be compared graphically by plotting total  $^{207}\text{Pb}/^{206}\text{Pb}$  vs. total  $^{204}\text{Pb}/^{206}\text{Pb}$   
419 covariation trends (Fig. 6). The slopes of the covariation trends are markedly different, with the  
420 steeper slope for the LA-ICP-MS data arising from the systematically lower  $^{204}\text{Pb}/^{206}\text{Pb}$  values  
421 and indicating lower  $^{204}\text{Pb}$  sensitivity relative to SHRIMP. On the other hand, the similar range  
422 of  $^{207}\text{Pb}/^{206}\text{Pb}$  measured by LA-ICP-MS and SHRIMP indicates that LA-ICP-MS-determined  
423  $^{207}\text{Pb}/^{206}\text{Pb}$  ratios are unaffected by differential Pb isotope sensitivity in these samples. Note that  
424 for the purposes of this discussion, the term Pb sensitivity includes the effects of instrument  
425 sensitivity, the  $^{204}\text{Hg}$  interference correction applied to LA-ICP-MS-measured ratios, and  
426 downhole Pb isotope fractionation. Because LA-ICP-MS  $^{204}\text{Pb}/^{206}\text{Pb}$  ratios but not  $^{207}\text{Pb}/^{206}\text{Pb}$   
427 ratios are affected, correction for  $^{204}\text{Hg}$ , which affects only the  $^{204}\text{Pb}/^{206}\text{Pb}$  ratio, seems a likely  
428 culprit for creating a differential Pb isotope sensitivity problem. This comparison suggests  
429 cautious application of  $^{204}\text{Hg}$  corrections to LA-ICP-MS data for high  $\text{Pb}_i$  phases and use of the  
430 207 method if differential Pb isotope sensitivity is suspected.

431

### 432 **U-Pb isochron evolution on the Tera-Wasserburg (semi-total Pb/U) diagram**

433 Ideally, when a set of titanite grains or domains crystallizes at the same time, the U-Pb  
434 data for this population will define sloped linear arrays in Tera-Wasserburg space. Such arrays  
435 are often referred to as discordia by analogy with the familiar Wetherill-diagram zircon discordia,  
436 which form as a result of changes to the U/Pb ratio due to open-system U or Pb loss. In titanite  
437 with no  $\text{Pb}_i$ , open-system modification of the U/Pb ratio would also produce a sloped, discordant

438 array of data (Tera and Wasserburg 1974; Schoene 2014). However, most titanite incorporates  
439  $Pb_i$ , and sloped, linear arrays are more often mixing arrays treated as isochrons resulting from  
440 variable  $U/Pb_i$  ratio ( $\mu$ ). If the data are precise and well-spaced (have a range of  $U/Pb_i$ ), then a  
441 regression provides a tightly constrained upper y-axis intercept at the shared  $Pb_i$   $^{207}Pb/^{206}Pb$   
442 value and lower intercept with the Tera-Wasserburg concordia at the age of crystallization.

443 The Tera-Wasserburg concordia is the locus of the time-integrated  $^{207}Pb/^{206}Pb$  and  
444  $^{238}U/^{206}Pb$  ratios resulting from U decay in the absence of  $Pb_i$ ; each point along the concordia is  
445 an implicit function of initial  $^{235}U/^{238}U$ , and thus time of crystallization. Paths in Figure 7A show  
446 the temporal evolution of radiogenic  $^{207}Pb/^{206}Pb$  and  $^{238}U/^{206}Pb$  ratios for several initial  $^{235}U/^{238}U$   
447 ratios. For titanite crystallized since  $\sim 3.0$  Ga, the temporal evolution paths are nearly parallel to  
448 the  $^{238}U/^{206}Pb$  axis because of the much greater relative change in  $^{238}U/^{206}Pb$  as compared to  
449  $^{207}Pb/^{206}Pb$  during radiogenic Pb ingrowth.

450 The addition of  $Pb_i$  to titanite constrains the starting points of the temporal evolution  
451 paths to a fixed  $^{207}Pb/^{206}Pb$  value (Fig. 7B). The shapes of the evolution paths depend on the  
452 evolving relative proportions of  $Pb_i$  with a fixed  $^{207}Pb/^{206}Pb$  composition and radiogenic Pb,  
453 growing in with a time-varying  $^{207}Pb/^{206}Pb$  composition (Fig. 7B, pale gray curves). For  
454 proportionally higher  $Pb_i$ , evolution paths are steeper, reflecting the dominance of the fixed  
455  $^{207}Pb/^{206}Pb$  value of the  $Pb_i$ . For lower  $Pb_i$ , evolution paths are shallower, reflecting dominance  
456 of the time-varying radiogenic  $^{207}Pb/^{206}Pb$  ratio. Titanite domains that crystallize at the same  
457 time and have remained closed throughout their evolution but contain varying concentrations of  
458  $Pb_i$  will defined a mixing line between the  $Pb_i$  composition and the radiogenic Pb composition at  
459 any given time. This mixing line will evolve in a systematic way with time, sweeping toward  
460 lower  $^{207}Pb/^{206}Pb$  and  $^{238}U/^{206}Pb$ , and is thus an isochron (Fig. 7B, dark gray lines). When the  $Pb_i$

461 composition incorporated into titanite has a lower  $^{207}\text{Pb}/^{206}\text{Pb}$ , the initial Pb-radiogenic Pb  
462 mixing line and the resulting isochrons will have shallower slopes (Fig. 7C, blue lines).  
463 Consequently, linear arrays of titanite U-Pb data that show changes in slope (curve or bend) or  
464 appear to intersect with other linear arrays are indicative of changes in  $\text{Pb}_i$  composition during  
465 crystallization or recrystallization.

466 Fractionation of U and Pb results in titanite with variable U/Pb ratio and can arise from  
467 differential mobility of these elements during crystallization, recrystallization or intragrain  
468 diffusion. In titanite that also incorporates  $\text{Pb}_i$ , fractionation of U and Pb manifests as  
469 subhorizontal data arrays that approximately parallel the  $^{238}\text{U}/^{206}\text{Pb}$  axis on the Terra-Wasserburg  
470 diagram (Fig. 7D, E). Changes in U/Pb ratio that occur long after initial titanite crystallization  
471 should generate more horizontal arrays than changes to U/Pb ratios that occur shortly after  
472 crystallization (Fig. 7E; Tera and Wasserburg, 1974) because  $\text{Pb}_i$  makes up a larger proportion  
473 of total Pb in titanite early on. Pb loss can occur by Pb diffusion or by recrystallization that  
474 produces a higher U/Pb ratio than present in earlier-formed titanite. Significant U diffusion in  
475 titanite is unlikely (Frost et al., 2000); however, real or apparent U loss can occur when  
476 recrystallization produces a lower U/Pb ratio than present in earlier-formed titanite. Significant U  
477 loss can produce reverse discordance on the Tera-Wasserburg diagram (Fig. 7D).

478 Pb isotopic fractionation during diffusion is expected to be negligible because of the  
479 small relative mass differences between Pb isotopes. Pb isotopic variations during  
480 recrystallization will also be negligible in the case that earlier-formed titanite is the primary  
481 source of Pb to later-formed titanite (e.g., interface coupled dissolution-precipitation  
482 recrystallization of Holder and Hacker (2019)). Significant changes to both the U/Pb and Pb/Pb  
483 ratios of titanite are anticipated when recrystallization occurs in the presence of fluids that are

484 not in equilibrium with respect to the titanite-stabilizing phase assemblage – i.e. fluids external to  
485 the local rock system.

486

### 487 **Interpretation of the Harrisville titanite data from Tera-Wasserburg data patterns**

488 The curvature in Adirondack titanite U-Pb data arrays suggest variation in  $Pb_i$   
489 composition. Both LA-ICP-MS and SHRIMP data show an approximately linear trend with a  
490 slight curvature toward lower slope at  $^{207}Pb/^{206}Pb \sim 0.12$  (Fig. 2). This is expressed by a small  
491 offset of some Type-3 and Type-4 data relative to Type-1 and Type-2 data, as well as by greater  
492 dispersion of data within Type-3 and Type-4 grains relative to Type-2 grains (Fig. 3). Departure  
493 from a single linear isochron is also supported by the lack of a three-dimensional model solution  
494 for the aggregate data sets (Table 1). The curvature of the Adirondack data arrays suggests that  
495 titanite incorporated at least two different compositions of  $Pb_i$ , as do linear regressions that  
496 project toward varied  $Pb_i$   $^{207}Pb/^{206}Pb$  values, some of which are significantly lower than  $\sim 0.92$   
497 (Table 1). The subtlety of the array curvature makes defining linear segments by eye and  
498 dividing the data into  $Pb_i$  compositional groups challenging and potentially quite arbitrary.  
499 Differences in  $Pb_i$  composition can arise from variations in growth or recrystallization  
500 environment (Bonamici et al., 2015; Kohn, 2017; Lucassen et al., 2011; Marsh and Smye, 2017;  
501 Romer and Rötzler, 2003; Scibiorski et al., 2019), which should also be reflected in other  
502 compositional proxies, such as REE content,  $\delta^{18}O$ , or Th/U ratio. Thus, additional compositional  
503 information might be used to identify and define data populations that can appropriately be  
504 regressed together.

505 In addition to multiple  $Pb_i$  components, titanite U-Pb data also show evidence for Pb loss.  
506 For a given  $^{207}Pb/^{206}Pb$  ratio, U-Pb data are dispersed subparallel to the  $^{238}U/^{206}Pb$  axis (Fig. 8).

507 The  $^{204}\text{Pb}/^{206}\text{Pb}$  ratio decreases toward the concordia (Fig. 8A), but for a given  $^{204}\text{Pb}/^{206}\text{Pb}$  value,  
508 the  $^{204}\text{Pb}$ -corrected dates decrease systematically parallel to the  $^{238}\text{U}/^{206}\text{Pb}$  axis (Fig. 8B). This  
509 subhorizontal date gradient is consistent with Pb loss altering the  $^{238}\text{U}/^{206}\text{Pb}$  ratio (Fig. 7D, E).  
510 Diffusive Pb loss has been suggested for these grains based on previous work demonstrating  
511 diffusion of oxygen isotopes, which have similar diffusivity to Pb at granulite facies conditions  
512 (Cherniak, 1993; Zhang et al., 2006), and a lack of correlation between chemical and isotopic  
513 zoning in the Harrisville grains (Bonamici et al., 2014; 2015).

514 A quantitative model of Pb ingrowth and Pb loss can be constructed to approximate the  
515 Harrisville titanite history (Fig. 9; Supplemental Materials). It shows that significant Pb loss  
516 ~100 m.y. after initial titanite crystallization produces data scatter that is consistent with both the  
517 direction and magnitude of offset of Harrisville U-Pb data relative to a 1150-Ma isochron (cf. Fig.  
518 8). The model predicts that more recent Pb loss would have shifted the U-Pb data toward  
519 significantly higher  $^{238}\text{U}/^{206}\text{Pb}$  than observed. Thus, the relatively small, subhorizontal dispersion  
520 of U-Pb data on the Tera-Wasserburg diagram is consistent with magmatic titanite crystallization  
521 at ca. 1160 Ma followed by Pb loss during granulite-facies metamorphism at ca. 1050 Ma.

522

### 523 **Implications for interpreting (*in situ*) U-Pb titanite data**

524 Generalizing the geometric considerations of the Tera-Wasserburg diagram and the  
525 results from the Harrisville titanite example, U-Pb data patterns can be used to recognize both  
526  $\text{Pb}_i$  compositional variations on the grain scale and open-system U/Pb fractionation. Previous  
527 workers have long understood that data that form sloped linear arrays indicate a shared  $\text{Pb}_i$   
528 composition and isochronous formation (Ludwig, 1998; Storey et al., 2006; Tera and  
529 Wasserburg, 1972; 1974). Indeed, these types of datasets were the motivation for the

530 development of the Tera-Wasserburg diagram. In many cases, linear data arrays can be  
531 appropriately regressed to find both the shared, single crystallization age and  $Pb_i$  composition  
532 (e.g., Stearns et al., 2016; Marsh and Smye, 2017).

533 In contrast, intersecting and/or curved arrays (e.g., Kirkland et al., 2016) suggest non-  
534 isochronous (re)crystallization and variations in the  $Pb_i$  composition. Ideally, if distinct linear  
535 segments can be recognized within a curved array, the subset of data defining a given segment  
536 can be regressed to find an isochron. This analysis also suggests that curved arrays with  
537 progressively shallower slopes toward the right, toward higher U/Pb, on the Tera-Wasserburg  
538 diagram, are expected because ingrowth of radiogenic Pb over time potentially supplies an  
539 increasing radiogenic component to the  $Pb_i$  being incorporated into newly (re)crystallized titanite.

540 Data arrays that are dispersed parallel to the  $^{238}U/^{206}Pb$  axis (e.g., Scibiorski et al., 2019)  
541 suggest open-system alteration of the U/Pb ratio in an existing titanite grain by diffusion or  
542 (re)crystallization, possibly in the presence of a variable-composition fluid. In general,  
543 horizontally dispersed data should be treated with caution in choosing isochron regressions  
544 because data may have been shifted toward either lower or higher  $^{238}U/^{206}Pb$  by open-system  
545 U/Pb fractionation. Depending on the length scale of U or Pb mobility,  $^{238}U/^{206}Pb$  may be shifted  
546 to both higher *and* lower values within the same grain (i.e., dispersed horizontally away from the  
547 central, true isochron location). Bidirectional dispersal would be expected in the case that Pb  
548 diffusion depletes Pb from some regions of a grain while enriching other regions. Our results  
549 also suggest that reversely discordant points (data that fall to the left of the Tera-Wasserburg  
550 concordia) have been shifted subparallel to the  $^{238}U/^{206}Pb$  axis as a result of open-system  
551 recrystallization that decreases the U/Pb ratio.



552 In some cases, a subset of titanite U-Pb data form a linear array that can be regressed with  
553 the isochron method whereas other data fall significantly off the linear array (e.g., Garber et al.  
554 2017). Analyses that do not form part of the linear isochron array represent titanite domains that,  
555 relative to the data that define the linear isochron array, have incorporated a different  $Pb_i$   
556 composition, (re)crystallized at a different time, or a combination of both. These patterns cannot  
557 be created by simple variations in the relative proportions of the same  $Pb_i$  and radiogenic Pb  
558 between analyses.

559 Finally, data that form a cloud above concordia without well defined, linear or curvilinear,  
560 sloped or horizontal, arrays (e.g., Kohn and Corrie, 2011; Garber et al., 2017) reflect some  
561 combination of U/Pb fractionation, changing  $Pb_i$  composition, and/or variable crystallization age  
562 during titanite formation. Interpretation of age significance from such datasets requires additional  
563 geologic, petrologic, and microstructural constraints and/or a prior knowledge of expected age  
564 populations.

565

566

### Implications

567 Titanite is an opportunistic mineral with highly adaptive crystal chemistry (e.g., Frost et  
568 al., 2001; Kohn, 2017), and, as yet, the connections between titanite trace element content and  
569 titanite (re)crystallization environment remain only partially explored, especially in subsolidus  
570 hydrothermally altered and/or metamorphic titanite. Multiple processes can apparently produce  
571 similar trace element variations and patterns in titanite. For instance, microscale intragrain  
572 variations in high field strength elements have been linked to fine-scale fluid composition  
573 variations (Lucassen et al., 2010a; 2010b; 2011; Gao et al., 2012; Chen et al., 2016), sector  
574 zoning and trace element entrapment during growth (Hayden et al., 2008; Kohn, 2017), and

575 equilibrium or disequilibrium dissolution-reprecipitation processes (Romer and Rötzler, 2003;  
576 Olierook et al., 2018; Hartnady et al., 2019; Holder and Hacker, 2019). Trends in titanite rare  
577 earth element and actinide contents have also been linked to dissolution-reprecipitation (Garber  
578 et al., 2017), as well as to coeval allanite or garnet growth (Garber et al., 2017; Scibiorski et al.,  
579 2019), and sector zoning (Kohn, 2017; Bruand et al., 2019). Collectively, these studies suggest  
580 that titanite chemistry can record equilibrium trace-element partitioning, especially between  
581 titanite and melt, but that equilibrium may be very local (at the scale of grains) and/or that  
582 titanite can reflect kinetic limitations on element mobility, attachment, or detachment.  
583 Approaches like the Tera-Wasserburg analysis utilized in this study help to reduce the effect of  
584 these poorly understood controls on the interpretation of U-Pb systematics by allowing Pb<sub>i</sub>  
585 variations to be distinguished from U/Pb ratio variations, regardless of the exact process(es)  
586 responsible.

587         Moreover, when combined with grain-scale characterization of element and isotopic  
588 zoning, the Tera-Wasserburg-based analysis of this study demonstrates an approach for  
589 maximizing geochronologic information obtained by *in situ* U-Pb titanite analysis, especially for  
590 rocks with polyphase thermal histories. The approach described here also aids in identifying  
591 sources of uncertainty in U-Pb data, whether arising from the analysis itself or from actual  
592 geological variability. Even when precise dates are not recovered, geological processes and  
593 events that cause data scatter can be recognized through analysis of U-Pb data patterns using the  
594 Tera-Wasserburg diagram.

595

596

## Acknowledgements

597 We thank C. Mark Fanning of the Research School of Earth Sciences at the Australian National  
598 University for enabling SHRIMP U-Th-Pb data collection. We thank Nicki Geisler and Mark  
599 Pecha of the Arizona Laserchron Center for supporting LA-ICP-MS U-Th-Pb analysis and  
600 providing data analysis spreadsheets. Brian Hess expertly prepared samples. This work was  
601 supported through the National Science Foundation [grant number EAR-0838058] (award to  
602 John Valley). We also thank two anonymous reviewers for useful comments and suggestions for  
603 the improvement of this manuscript.

## References Cited

- 604  
605 Aleinikoff, J.N., Wintsch, R.P., Fanning, C.M., and Dorais, M.J. (2002) U–Pb geochronology of  
606 zircon and polygenetic titanite from the Glastonbury Complex, Connecticut, USA: an  
607 integrated SEM, EMPA, TIMS, and SHRIMP study. *Chemical Geology*, 188, 125–147.
- 608 Aleinikoff, J.N., Horton, J.W., Drake, A.A., Wintsch, R.P., Fanning, C.M., and Yi, K. (2004)  
609 Deciphering multiple Mesoproterozoic and Paleozoic events recorded in zircon and  
610 titanite from the Baltimore Gneiss, Maryland: SEM imaging, SHRIMP U-Pb  
611 geochronology, and EMP analysis. In *Proterozoic Tectonic Evolution of the Grenville  
612 Orogen in North America Vol. 197*, pp. 411–434. Geological Society of America.
- 613 Aleinikoff, J.N., Wintsch, R.P., Tollo, R.P., Unruh, D.M., Fanning, C.M., and Schmitz, M.D.  
614 (2007) Ages and origins of rocks of the Killingworth dome, south-central Connecticut:  
615 Implications for the tectonic evolution of southern New England. *American Journal of  
616 Science*, 307, 63–118.
- 617 Amelin, Y. (2009) Sm–Nd and U–Pb systematics of single titanite grains. *Chemical Geology*,  
618 261, 53–61.
- 619 Baird, G.B., and MacDonald, W.D. (2004) Deformation of the Diana syenite and Carthage-  
620 Colton mylonite zone: Implications for timing of Adirondack Lowlands deformation. In  
621 *Memoir 197: Proterozoic Tectonic Evolution of the Grenville Orogen in North America  
622 Vol. 197*, pp. 285–297. Geological Society of America.
- 623 Bonamici, C.E., Kozdon, R., Ushikubo, T., and Valley, J.W. (2014) Intragrain oxygen isotope  
624 zoning in titanite by SIMS: Cooling rates and fluid infiltration along the Carthage-Colton  
625 Mylonite Zone, Adirondack Mountains, NY, USA. *Journal of Metamorphic Geology*, 32,  
626 71–92.

- 627 Bonamici, C.E., Fanning, C.M., Kozdon, R., Fournelle, J.H., and Valley, J.W. (2015) Combined  
628 oxygen-isotope and U-Pb zoning studies of titanite: New criteria for age preservation.  
629 Chemical Geology, 398, 70–84.
- 630 Butler, R.F., Gehrels, G.E., Baldwin, S.L., and Davidson, C. (2002) Paleomagnetism and  
631 geochronology of the Ecstall pluton in the Coast Mountains of British Columbia: Evidence  
632 for local deformation rather than large-scale transport. Journal of Geophysical Research:  
633 Solid Earth, 107, EPM 3-1.
- 634 Bruand, E., Storey, C., Fowler, M., and Heilimo, E. (2019) Oxygen isotopes in titanite and  
635 apatite, and their potential for crustal evolution research. Geochimica et Cosmochimica  
636 Acta, 255, 144–162.
- 637 Cartwright, I., Valley, J., and Hazelwood, A.-M. (1993) Resetting of oxybarometers and oxygen  
638 isotope ratios in granulite facies orthogneisses during cooling and shearing, Adirondack  
639 Mountains, New York. Contributions to Mineralogy and Petrology, 113, 208–225.
- 640 Chen, Y.-X., Zhou, K., Zheng, Y.-F., Gao, X.-Y., and Yang, Y.H. (2016) Polygenetic titanite  
641 records the composition of metamorphic fluids during the exhumation of ultrahigh-  
642 pressure metagranite in the Sulu orogen. Journal of Metamorphic Geology, 34, 573–594.
- 643 Cherniak, D.J. (1993) Lead diffusion in titanite and preliminary results on the effects of radiation  
644 damage on Pb transport. Chemical Geology, 110, 177–194.
- 645 ——— (2010) Diffusion in Accessory Minerals: Zircon, Titanite, Apatite, Monazite and  
646 Xenotime. Reviews in Mineralogy and Geochemistry, 72, 827–869.
- 647 Chew, D.M., Petrus, J.A., and Kamber, B.S. (2014) U–Pb LA–ICPMS dating using accessory  
648 mineral standards with variable common Pb. Chemical Geology, 363, 185–199.

- 649 DeWolf, C.P., and Mezger, K. (1994) Lead isotope analyses of leached feldspars: Constraints on  
650 the early crustal history of the Grenville Orogen. *Geochimica et Cosmochimica Acta*, 58,  
651 5537–5550.
- 652 Essex, R.M., and Gromet, L.P. (2000) U-Pb dating of prograde and retrograde titanite growth  
653 during the Scandian orogeny. *Geology*, 28, 419–422.
- 654 Frost, B.R., Chamberlain, K.R., and Schumacher, J.C. (2001) Sphene (titanite): phase relations  
655 and role as a geochronometer. *Chemical Geology*, 172, 131–148.
- 656 Gao, X.-Y., Zheng, Y.-F., Chen, Y.-X., and Guo, J. (2012) Geochemical and U–Pb age  
657 constraints on the occurrence of polygenetic titanites in UHP metagranite in the Dabie  
658 orogen. *Lithos*, 136–139, 93–108.
- 659 Garber, J.M., Hacker, B.R., Kylander-Clark, A.R.C., Stearns, M., and Seward, G. (2017)  
660 Controls on Trace Element Uptake in Metamorphic Titanite: Implications for  
661 Petrochronology. *Journal of Petrology*, 58, 1031–1057.
- 662 Gehrels, G.E., Valencia, V.A., and Ruiz, J. (2008) Enhanced precision, accuracy, efficiency, and  
663 spatial resolution of U-Pb ages by laser ablation–multicollector–inductively coupled  
664 plasma–mass spectrometry. *Geochemistry, Geophysics, Geosystems*, 9.
- 665  
666 Gulson, B.L. (1984) Uranium-lead and lead-lead investigations of minerals from the Broken Hill  
667 lodes and mine sequence rocks. *Economic Geology*, 79, 476–490.
- 668 Hartnady, M.I.H., Kirkland, C.L., Clark, C., Spaggiari, C.V., Smithies, R.H., Evans, N.J., and  
669 McDonald, B.J. (2019) Titanite dates crystallisation; slow Pb diffusion during super-  
670 solidus re-equilibration. *Journal of Metamorphic Geology*, 37, 823–838.
- 671 Heumann, Matthew J. (2004) Thermochronological and Geochronological studies in the  
672 Adirondack Highlands and Lowlands, New York. Syracuse University.

- 673 Holder, R.M., and Hacker, B.R. (2019) Fluid-driven resetting of titanite following ultrahigh-  
674 temperature metamorphism in southern Madagascar. *Chemical Geology*, 504, 38–52.
- 675 Horstwood, M.S., L. Foster, G., R. Parrish, R., R. Noble, S., and M. Nowell, G. (2003)  
676 Common-Pb corrected *in situ* U–Pb accessory mineral geochronology by LA-MC-ICP-  
677 MS. *Journal of Analytical Atomic Spectrometry*, 18, 837–846.
- 678 Ireland, T.R., and Williams, I.S. (2003) Considerations in Zircon Geochronology by SIMS.  
679 *Reviews in Mineralogy and Geochemistry*, 53, 215–242.
- 680 Johnson, E.L., Goergen, E.T., and Fruchey, B.L. (2004) Right lateral oblique slip movements  
681 followed by post-Ottawan (1050–1020 Ma) orogenic collapse along the Carthage-Colton  
682 shear zone: Data from the Dana Hill metagabbro body, Adirondack Mountains, New  
683 York. In *Memoir 197: Proterozoic Tectonic Evolution of the Grenville Orogen in North*  
684 *America Vol. 197*, pp. 357–378. Geological Society of America.
- 685 Johnson, E.L., Selleck, B.W., DeLorraine, B., and Lupulescu, M. (2005) The nature and  
686 significance of the Carthage-Colton shear zone and related late-to-post tectonic granites  
687 and ore deposits. *Friends of the Grenville*.
- 688 Jung, S., and Hellebrand, E. (2007) Textural, geochronological and chemical constraints from  
689 polygenetic titanite and monogenetic apatite from a mid-crustal shear zone: An integrated  
690 EPMA, SIMS, and TIMS study. *Chemical Geology*, 241, 88–107.
- 691 Kirkland, C.L., Spaggiari, C.V., Johnson, T.E., Smithies, R.H., Danišik, M., Evans, N., Wingate,  
692 M.T.D., Clark, C., Spencer, C., Mikucki, E., and others (2016) Grain size matters:  
693 Implications for element and isotopic mobility in titanite. *Precambrian Research*, 278,  
694 283–302.

- 695 Kirkland, C.L., Hollis, J., Danišik, M., Petersen, J., Evans, N.J., and McDonald, B.J. (2017)  
696 Apatite and titanite from the Karrat Group, Greenland; implications for charting the  
697 thermal evolution of crust from the U-Pb geochronology of common Pb bearing phases.  
698 Precambrian Research, 300, 107–120.
- 699 Kohn, M.J. (2017) Titanite Petrochronology. Reviews in Mineralogy and Geochemistry, 83,  
700 419–441.
- 701 Kohn, M.J., and Corrie, S.L. (2011) Preserved Zr-temperatures and U–Pb ages in high-grade  
702 metamorphic titanite: Evidence for a static hot channel in the Himalayan orogen. Earth  
703 and Planetary Science Letters, 311, 136–143.
- 704 Lamb, W.M. (1993) Retrograde deformation within the Carthage-Colton Zone as recorded by  
705 fluid inclusions and feldspar compositions: tectonic implications for the southern  
706 Grenville Province. Contributions to Mineralogy and Petrology, 114, 379–394.
- 707 Li, J.-W., Deng, X.-D., Zhou, M.-F., Liu, Y.-S., Zhao, X.-F., and Guo, J.-L. (2010) Laser  
708 ablation ICP-MS titanite U–Th–Pb dating of hydrothermal ore deposits: A case study of  
709 the Tonglushan Cu–Fe–Au skarn deposit, SE Hubei Province, China. Chemical Geology,  
710 270, 56–67.
- 711 Lucassen, F., Dulski, P., Abart, R., Franz, G., Rhede, D., and Romer, R.L. (2010a) Redistribution  
712 of HFSE elements during rutile replacement by titanite. Contributions to Mineralogy and  
713 Petrology, 160, 279–295.
- 714 Lucassen, F., Franz, G., Rhede, D., and Wirth, R. (2010b) Ti-Al zoning of experimentally grown  
715 titanite in the system CaO-Al<sub>2</sub>O<sub>3</sub>-TiO<sub>2</sub>-SiO<sub>2</sub>-NaCl-H<sub>2</sub>O-(F): Evidence for small-scale  
716 fluid heterogeneity. American Mineralogist, 95, 1365.



- 717 Lucassen, F., Franz, G., Dulski, P., Romer, R.L., and Rhede, D. (2011) Element and Sr isotope  
718 signatures of titanite as indicator of variable fluid composition in hydrated eclogite.  
719 *Lithos*, 121, 12–24.
- 720 Ludwig, K.R. (1998) On the Treatment of Concordant Uranium-Lead Ages. *Geochimica et*  
721 *Cosmochimica Acta*, 62, 665–676.
- 722 Ludwig, K. (2009) SQUID 2: A User's Manual, rev. 12 Apr, 2009, 110 p.
- 723 Ludwig, K.R. (2012) User's Manual for Isoplot 3.75: A Geochronological Toolkit for Microsoft  
724 Excel, 75 p.
- 725 Marsh, J.H., and Smye, A.J. (2017) U-Pb systematics and trace element characteristics in titanite  
726 from a high-pressure mafic granulite. *Chemical Geology*, 466, 403–416.
- 727 McGregor, M., McFarlane, C.R.M., and Spray, J.G. (2019) In situ multiphase U–Pb  
728 geochronology and shock analysis of apatite, titanite and zircon from the Lac La Moinerie  
729 impact structure, Canada. *Contributions to Mineralogy and Petrology*, 174, 62.
- 730 McLelland, J.M., Selleck, B.W., and Bickford, M.E. (2010) Review of the Proterozoic evolution  
731 of the Grenville Province, its Adirondack outlier, and the Mesoproterozoic inliers of the  
732 Appalachians. *Geological Society of America Memoirs*, 206, 21–49.
- 733 Mezger, K., Pluijm, B. a. V.D., Essene, E.J., and Halliday, A.N. (1991a) Synorogenic Collapse:  
734 A Perspective from the Middle Crust, the Proterozoic Grenville Orogen. *Science*, 254,  
735 695–698.
- 736 Mezger, K., Rawnsley, C.M., Bohlen, S.R., and Hanson, G.N. (1991b) U-Pb Garnet, Spinel,  
737 Monazite, and Rutile Ages: Implications for the Duration of High-Grade Metamorphism  
738 and Cooling Histories, Adirondack Mts., New York. *The Journal of Geology*, 99, 415–  
739 428.

- 740 Mezger, K., Pluijm, B.A. van der, Essene, E.J., and Halliday, A.N. (1992) The Carthage-Colton  
741 Mylonite Zone (Adirondack Mountains, New York): The Site of a Cryptic Suture in the  
742 Grenville Orogen? *The Journal of Geology*, 100, 630–638.
- 743 Mezger, K., Essene, E.J., van der Pluijm, B.A., and Halliday, A.N. (1993) U-Pb geochronology  
744 of the Grenville Orogen of Ontario and New York: constraints on ancient crustal  
745 tectonics. *Contributions to Mineralogy and Petrology*, 114, 13–26.
- 746 Olierook, H.K.H., Taylor, R.J.M., Erickson, T.M., Clark, C., Reddy, S.M., Kirkland, C.L., Jahn,  
747 I., and Barham, M. (2019) Unravelling complex geologic histories using U–Pb and trace  
748 element systematics of titanite. *Chemical Geology*, 504, 105–122.
- 749 Papapavlou, K., Darling, J.R., Storey, C.D., Lightfoot, P.C., Moser, D.E., and Lasalle, S. (2017)  
750 Dating shear zones with plastically deformed titanite: New insights into the orogenic  
751 evolution of the Sudbury impact structure (Ontario, Canada). *Precambrian Research*, 291,  
752 220–235.
- 753 Papapavlou, K., Darling, J.R., Moser, D.E., Barker, I.R., White, L.F., Lightfoot, P.C., Storey,  
754 C.D., Dunlop, J., and EIMF (2018) U–Pb isotopic dating of titanite microstructures:  
755 potential implications for the chronology and identification of large impact structures.  
756 *Contributions to Mineralogy and Petrology*, 173, 82.
- 757 Prowatke, S., and Klemme, S. (2005) Effect of melt composition on the partitioning of trace  
758 elements between titanite and silicate melt. *Geochimica et Cosmochimica Acta*, 69, 695–  
759 709.
- 760 Romer, R.L., and Rötzler, J. (2003) Effect of metamorphic reaction history on the U-Pb dating of  
761 titanite. *Geological Society, London, Special Publications*, 220, 147–158.

- 762 Rubatto, D., and Scambelluri, M. (2003) U-Pb dating of magmatic zircon and metamorphic  
763 baddeleyite in the Ligurian eclogites (Voltri Massif, Western Alps). *Contributions to*  
764 *Mineralogy and Petrology*, 146, 341–355.
- 765 Schoene, B. (2014) 4.10-U–Th–Pb Geochronology. *Treatise on Geochemistry*, 4, 341–378.
- 766 Scibiorski, E., Kirkland, C.L., Kemp, A.I.S., Tohver, E., and Evans, N.J. (2019) Trace elements  
767 in titanite: A potential tool to constrain polygenetic growth processes and timing.  
768 *Chemical Geology*, 509, 1–19.
- 769 Stacey, J.S., and Kramers, J.D. (1975) Approximation of terrestrial lead isotope evolution by a  
770 two-stage model. *Earth and Planetary Science Letters*, 26, 207–221.
- 771 Stearns, M.A., Hacker, B.R., Ratschbacher, L., Rutte, D., and Kylander-Clark, A.R.C. (2015)  
772 Titanite petrochronology of the Pamir gneiss domes: Implications for middle to deep  
773 crust exhumation and titanite closure to Pb and Zr diffusion. *Tectonics*, 34, 784–802.
- 774 Stearns, M.A., Cottle, J.M., Hacker, B.R., and Kylander-Clark, A.R.C. (2016) Extracting thermal  
775 histories from the near-rim zoning in titanite using coupled U-Pb and trace-element depth  
776 profiles by single-shot laser-ablation split stream (SS-LASS) ICP-MS. *Chemical Geology*,  
777 422, 13–24.
- 778 Stern, Robert (1997) The GSC sensitive high resolution ion microprobe (SHRIMP): analytical  
779 techniques of zircon U–Th–Pb age determinations and performance evaluation.  
780 *Geological Survey of Canada Report*, 10, 1–31.
- 781 Storey, C.D., Jeffries, T.E., and Smith, M. (2006) Common lead-corrected laser ablation ICP–  
782 MS U–Pb systematics and geochronology of titanite. *Chemical Geology*, 227, 37–52.

- 783 Storey, C.D., Smith, M.P., and Jeffries, T.E. (2007) *In situ* LA-ICP-MS U–Pb dating of  
784 metavolcanics of Norrbotten, Sweden: Records of extended geological histories in  
785 complex titanite grains. *Chemical Geology*, 240, 163–181.
- 786 Streepey, M., E. L. Johnson, K. Mezger, and B. A. van der Pluijm (2001) Early History of the  
787 Carthage-Colton Shear Zone, Grenville Province, Northwest Adirondacks, New York  
788 (U.S.A.). *The Journal of Geology*, 109, 479–492.
- 789 Tera, F., and Wasserburg, G.J. (1972) U-Th-Pb systematics in three Apollo 14 basalts and the  
790 problem of initial Pb in lunar rocks. *Earth and Planetary Science Letters*, 14, 281–304.
- 791 Tera, F., and Wasserburg, G.J. (1974) U-Th-Pb systematics on lunar rocks and inferences about  
792 lunar evolution and the age of the moon. In *Lunar and Planetary Science Conference*  
793 *Proceedings Vol. 5*, pp. 1571–1599.
- 794 Tiepolo, M., Oberti, R., and Vannucci, R. (2002) Trace-element incorporation in titanite:  
795 constraints from experimentally determined solid/liquid partition coefficients. *Chemical*  
796 *Geology*, 191, 105–119.
- 797 Timms, N.E., Pearce, M.A., Erickson, T.M., Cavosie, A.J., Rae, Auriol S. P., Wheeler, J.,  
798 Wittmann, Axel, Ferrière, Ludovic, Poelchau, Michael H., Tomioka, Naotaka, and others  
799 (2019) New shock microstructures in titanite (CaTiSiO<sub>5</sub>) from the peak ring of the  
800 Chicxulub impact structure, Mexico. *Contributions to Mineralogy and Petrology*, 174, 38.
- 801 Verts, L.A., Chamberlain, K.R., and Frost, C.D. (1996) U-Pb sphene dating of metamorphism:  
802 the importance of sphene growth in the contact aureole of the Red Mountain pluton,  
803 Laramie Mountains, Wyoming. *Contributions to Mineralogy and Petrology*, 125, 186–  
804 199.

- 805 Williams, I.S. (1998) U-Th-Pb geochronology by ion microprobe. *Reviews in Economic*  
806 *Geology*, 7, 1–35.
- 807 Wohlgemuth-Ueberwasser, C.C., Tegner, C., and Pease, V. (2017) LA-Q-ICP-MS apatite U/Pb  
808 geochronology using common Pb in plagioclase: Examples from layered mafic intrusions.  
809 *American Mineralogist*, 102, 571–579.
- 810 Zhang, X.Y., Cherniak, D.J., and Watson, E.B. (2006) Oxygen diffusion in titanite: Lattice  
811 diffusion and fast-path diffusion in single crystals. *Chemical Geology*, 235, 105–123.
- 812

813 **Figure Captions**

814 Figure 1. Post-analysis images of U-Pb LA-ICP-MS and SHRIMP analysis pits at a similar scale.  
815 Both sets of analysis pits have similar diameters, 35-40  $\mu\text{m}$ . SHRIMP pits are 2-3  $\mu\text{m}$  deep; LA-  
816 ICP-MS pits are 15  $\mu\text{m}$  deep.

817  
818 Figure 2. Total LA-ICP-MS and SHRIMP U-Pb titanite datasets, colored by grain 'Type' as  
819 determined by microstructural setting (Bonamici et al., 2014; 2015). The LA-ICP-MS dataset is  
820 more extensive (n = 280) than the SHRIMP dataset (n = 101) because of the shorter analysis time.

821  
822 Figure 3. Total Pb/U plots for each Adirondack titanite grain. Grain designations are listed in  
823 upper right corner of each plot with the Type in parentheses behind. See Table 1 for grain Type  
824 explanations. LA-ICP-MS data shown in gray; SHRIMP data shown in black. Constrained 3D  
825 linear regressions are projected into the 2D space of the Tera-Wasserburg diagram. Lower  
826 concordia intercepts and MSWDs for constrained 3D and 2D regressions are given for each grain.  
827 Leftmost column contains Type-1 and -2 grains, which show generally small U/Pb ratio spread  
828 and highly clustered analyses. Center column contains Type-3 grains, which show greater U/Pb  
829 variations. The rightmost column contains Type-4 grains showing the largest spread in U/Pb  
830 ratios.

831  
832 Figure 4. Results of 3D linear isochron regressions (Ludwig, 2012) for individual Adirondack  
833 titanite grains, showing large uncertainties and relatively poor age constraints provided by this  
834 type of analysis. See also Figure 3 and Table 1. (A) Concordia-intercept ages and 2SD  
835 uncertainties from regressions with constrained  $\text{Pb}_i$   $^{207}\text{Pb}/^{206}\text{Pb}$ . Light gray fields show the

836 known age ranges for the Shawinigan and Ottawan phases of the Grenville orogenic cycle for  
837 reference. (B) Lower intercepts and 2SD uncertainties, in the Tera-Wasserburg plane, of  
838 unconstrained regressions. Within large uncertainties, all but one grain (HA12B) give lower  
839 intercepts the overlap concordia. All regressions of SHRIMP data return MSWD values greater  
840 than 2. Approximate ages for the Shawinigan and Ottawan phases are indicated on the concordia  
841 for reference.

842  
843 Figure 5. Comparison of individually  $Pb_i$ -corrected U-Pb dates for a subset of Adirondack  
844 titanite grains that were analyzed by both LA-ICP-MS and SHRIMP. Traverses show the spatial  
845 variations in  $Pb_i$ -corrected  $^{238}U/^{206}Pb$  dates. Profiles are generated using the preferred  $Pb_i$ -  
846 correction for each analytical technique—207 method for LA-ICP-MS and 204-method for  
847 SHRIMP. Vertical bars show average, external  $1\sigma$  uncertainties for SHRIMP (red) and LA-ICP-  
848 MS (blue). Dashed horizontal lines show mean concordia-intercept ages from 3D linear isochron  
849 regressions; note that uncertainties on these regression ages are not shown but are generally large  
850 (see Fig. 4). U-Pb profiles for all grains in this study can be found in Supplemental Figures S1  
851 through S13.

852  
853 Figure 6. Plot of total  $^{207}Pb/^{206}Pb$  vs. total  $^{204}Pb/^{206}Pb$  measured in Harrisville titanite by LA-  
854 ICP-MS (blue) and SHRIMP (red). See text for discussion.

855  
856 Figure 7. Schematic diagrams showing the behavior of U-Pb data on a Tera-Wasserburg diagram.  
857 (A) Selected paths showing the ingrowth of radiogenic Pb in the absence of  $Pb_i$  as function of  
858 various starting U isotope compositions. Topmost path shows ingrowth trajectory for a titanite

859 grain crystallized at the time of Earth formation with the primordial (meteoritic) U isotope  
860 composition. (B) Evolution of a mixing line (isochron) between  $Pb^*$  and  $Pb_i$  with  $^{207}Pb/^{206}Pb =$   
861 0.96. Black line with the steepest slope represents the present-day isochron. Gray lines with  
862 negative slopes show the position of the isochron at different arbitrary times during its evolution  
863 from its initial to its present-day position. Gray lines with positive slopes show ingrowth curves  
864 for  $Pb^*$  mixed with variable proportions of  $Pb_i$ .  $Pb_i$  composition is shown by the horizontal  
865 dashed line. (C) Same as B with a different isochron evolution superimposed (blue lines),  
866 demonstrating the effect of later titanite (re)crystallization with a different, more radiogenic  $Pb_i$   
867 ( $^{207}Pb/^{206}Pb = 0.6$ ). (D) Schematic representation of Pb ingrowth trajectories for titanite suffering  
868 open-system modification of its U/Pb ratio. Thin colored lines are normal ingrowth trajectories  
869 (with varying proportions of  $Pb_i$ ); heavier arrows simulate instantaneous change in U/Pb ratio by  
870 either recent or ancient open-system event. Subsequently, Pb ingrowth returns to closed-system  
871 behavior (thin lines). (E) Schematic representation of the U-Pb data arrays expected in the case  
872 of open-system U/Pb ratio modification, as demonstrated in D.

873  
874 Figure 8. U-Pb analyses with color scaling showing covariation with additional isotopic data. (A)  
875 SHRIMP data and (B) LA-ICP-MS data with color scaling showing total  $^{204}Pb/^{206}Pb$ . The  
876 transition from warm to cool colors toward concordia is consistent with decreasing relative  
877 abundance of  $Pb_i$ . (C) SHRIMP data and (D) LA-ICP-MS data with color scaling showing 204-  
878 corrected date. Comparison with A and B suggests that for a given  $^{204}Pb/^{206}Pb$  value ( $Pb_i$   
879 abundance), variation in  $Pb_i$ -corrected dates reflects variation in U/Pb ratio. Only Type 1 and  
880 Type 2 data, which retain evidence for oxygen isotope and Pb diffusion (Bonamici et al. 2014;  
881 2015), are shown in B and D.

882



883 Figure 9. Quantitative models showing the effect of Pb loss on U-Pb systematics for titanite with  
884  $Pb_i$  on the Terra-Wasserberg diagram. Model is constructed to simulate possible scenarios for the  
885 Harrisville titanite grains: initial crystallization at 1150 Ma with low  $Pb_i$  followed by Pb loss  
886 shortly after crystallization at 1050 Ma (orange curve) or Pb loss long after crystallization at 650  
887 Ma (green curve). Modeling details in Supplemental Materials. (A) Ingrowth curves showing full  
888 ingrowth trajectories, including Pb loss events. (B) Expanded region of A showing where  
889 evolution curves end (X's), relative to the 1150 Ma and 1050 Ma isochrons, and depending on  
890 the timing of Pb loss.  
891

## Appendix

892  
 893 Stacey and Kramers (1975) determined modern-day crustal average Pb isotope ratios to be  
 894  $^{206}\text{Pb}/^{204}\text{Pb} = 18.70$ ,  $^{207}\text{Pb}/^{204}\text{Pb} = 15.63$ , and  $^{208}\text{Pb}/^{204}\text{Pb} = 38.63$ , based on Pb isotopic data from  
 895 “conformable” galena. They then fitted a two-stage Pb evolution curve, the second stage having  
 896  $\mu = ^{238}\text{U}/^{204}\text{Pb} = 9.74$ . In practice,  $\text{Pb}_i$  ratios based on the Stacey and Kramers (1975) model can  
 897 be calculated for materials younger than 3.7 Ga from equations 1 and 2 below, using the modern-  
 898 day crustal average Pb isotope ratios and an approximate age (Stacey and Kramers model Pb  
 899 ratios are superscripted SK).

900

$$901 \quad \left( \frac{^{206}\text{Pb}}{^{204}\text{Pb}} \right)_i^{\text{SK}} = \left( \frac{^{206}\text{Pb}}{^{204}\text{Pb}} \right)_{\text{today}}^{\text{SK}} \left( e^{238t} - 1 \right) \quad [\text{eq.1}]$$

$$902 \quad \left( \frac{^{207}\text{Pb}}{^{204}\text{Pb}} \right)_i^{\text{SK}} = \left( \frac{^{207}\text{Pb}}{^{204}\text{Pb}} \right)_{\text{today}}^{\text{SK}} \frac{1}{137.82} \left( e^{235t} - 1 \right) \quad [\text{eq.2}]$$

903

904 The 204 method initial Pb correction (Stern, 1997) subtracts the initial Pb fraction ( $^{204c}f_{206}$ ),  
 905 calculated using Stacey and Kramers (1975)  $\text{Pb}_i$  ratios, from the total measured  $^{206}\text{Pb}/^{238}\text{U}$  to  
 906 determine the radiogenic  $^{206}\text{Pb}/^{238}\text{U}$  ratio.

$$907 \quad ^{204c}f_{206} = \frac{^{206}\text{Pb}_i}{^{206}\text{Pb}_{\text{total}}} = \frac{\left( \frac{^{204}\text{Pb}/^{206}\text{Pb}} \right)_{\text{measured}}^{\text{unknown}}}{\left( \frac{^{204}\text{Pb}/^{206}\text{Pb}} \right)_i^{\text{SK}}} \quad [\text{eq.3}]$$

$$908 \quad \left( \frac{^{206}\text{Pb}^*}{^{238}\text{U}} \right)_{\text{corrected}}^{\text{unknown}} = \left( 1 - ^{204c}f_{206} \right) \left( \frac{^{206}\text{Pb}}{^{238}\text{U}} \right)_{\text{measured}}^{\text{unknown}} \quad [\text{eq.4}]$$

909

910 The  $^{207}\text{Pb}$  method  $\text{Pb}_i$  correction (Stern, 1997) subtracts the initial  $\text{Pb}$  fraction ( $^{207c}f_{206}$ ), calculated  
 911 using Stacey and Kramers (1975)  $\text{Pb}_i$  values and a starting guess or “expected” radiogenic  
 912  $^{207}\text{Pb}/^{206}\text{Pb}$  ratio, from the total measured  $^{207}\text{Pb}/^{206}\text{Pb}$  to determine the corrected radiogenic  
 913  $^{207}\text{Pb}/^{206}\text{Pb}$  ratio.

$$914 \quad ^{207c}f_{206} = \frac{^{206}\text{Pb}_i}{^{206}\text{Pb}_{total}} = \frac{\left(\frac{^{206}\text{Pb}}{^{207}\text{Pb}}\right)_{measured}^{unknown} \left(\frac{^{206}\text{Pb}^*}{^{207}\text{Pb}^*}\right)_{expected}^{unknown}}{\left(\frac{^{206}\text{Pb}}{^{207}\text{Pb}}\right)_i^{SK} \left(\frac{^{206}\text{Pb}^*}{^{207}\text{Pb}^*}\right)_{expected}^{unknown}} \quad [eq.5]$$

$$915 \quad f_{207} = ^{207c}f_{206} \frac{\left(\frac{^{207}\text{Pb}/^{206}\text{Pb}}\right)_i^{SK}}{\left(\frac{^{207}\text{Pb}/^{206}\text{Pb}}\right)_{measured}^{unknown}} \quad [eq.6]$$

$$916 \quad \left(\frac{^{207}\text{Pb}^*}{^{206}\text{Pb}^*}\right)_{corrected}^{unknown} = \left(\frac{^{207}\text{Pb}}{^{206}\text{Pb}}\right)_{measured}^{unknown} \times \frac{(1 - f_{207})}{(1 - ^{207c}f_{206})} \quad [eq.7]$$

917

918

919

920

Table 1. Summary descriptions and interpretations of titanite types from Harrisville area from previous work.

Titanite Type	Microstructural and Zoning Description	Reference
1	<p>Anhedral grains (100-500 <math>\mu\text{m}</math>) within lenses of grain-size-reduced augite + quartz + oxides <math>\pm</math> hornblende that define local <math>S_1</math> protomylonitic fabric. Subtle oscillatory zoning in major, minor elements and Th/U. Core-to-rim decreasing <math>\delta^{18}\text{O}</math> of <math>\leq 0.8\%</math>.</p> <p><i>Interpretation:</i> Magmatic titanite crystallized in AMCG Diana syenite; solid-state grain-size reduction during Ottawaan deformation.</p>	Bonamici et al. 2011; 2014; 2015
2	<p>Rounded porphyroclasts (100-1300 <math>\mu\text{m}</math>) within local <math>S_2</math> shear zones. Some show subgrain development and/or recrystallization at margins. Some are transected by one set of thin deformation twins. Chemical zoning marked by small, step-like and oscillating changes in minor and trace elements and Th/U. Core-to-rim decreasing <math>\delta^{18}\text{O}</math> of <math>\leq 1.5\%</math>.</p> <p><i>Interpretation:</i> Late magmatic titanite crystallized in AMCG Diana syenite, sheared as porphyroclasts during Ottawaan deformation</p>	Mezger et al. 1992; Bonamici et al., 2014; 2015
3	<p>Anhedral/xenoblastic grains and grain aggregates (<math>\sim 500</math>-5000 <math>\mu\text{m}</math>) within veins that crosscut local <math>S_1</math> foliation and variably contain local <math>S_2</math> foliation. Grains commonly contain one or two sets of deformation twins. Veins vary in mineralogy but commonly contain augite, K-feldspar, apatite, scapolite, and other calcsilicate minerals in addition to titanite. Sharply oscillating zoning in minor and trace elements.</p> <p><i>Interpretation:</i> Vein titanite crystallized from alkaline fluids cross-cutting Diana metasyenite during Ottawaan deformation and metamorphism.</p>	Johnson et al. 2005; Heumann, 2006; Bonamici et al. 2014; 2015
4	<p>Xenoblastic grains partially overgrowing local <math>S_3</math> mylonitic fabric. Pronounced zoning marked by sharp changes in minor and trace elements and Th/U. Nearly uniform <math>\delta^{18}\text{O}</math> across grain interiors with increasing <math>\delta^{18}\text{O}</math> (up to 1‰) in outer grain domains, coincident with pronounced chemical zoning.</p> <p><i>Interpretation:</i> Magmatic titanite crystallized in AMCG Diana syenite; solid-state grain-size reduction during Ottawaan metamorphism and deformation; solid-state rim growth during waning Ottawaan metamorphism.</p>	Bonamici et al. 2014; 2105

Table 2. Total Pb/U (3D) isochron regressions of U-Pb titanite data and associated go

	Concordia Intercept Age (Ma)	$2\sigma \pm$ (Ma)	MSWD	Prob. of Fit	TW plane intercept 238/206 <sup>1</sup>
<b>TYPE 1</b>					
<i>HA12B</i>					
SHRIMP - uncon <sup>4</sup>			2.5	0	5.1
SHRIMP - BH con <sup>5</sup>	1251	460	3.5	0	
LAICPMS - uncon			0.2	0.999	4.78
LAICPMS - con <sup>6</sup>	1206	210	0.2	1	
<b>TYPE 2</b>					
<i>HA03A S1</i>					
SHRIMP - uncon			4.7	0	4.76
SHRIMP - BH con	1146	120	5.8	0	
LAICPMS - uncon			0.62	0.98	5.27
LAICPMS - con	1111	48	0.63	0.98	
<i>HA03A S2</i>					
SHRIMP - uncon			3	0	4.4
SHRIMP - con	1182	390	3.1	0	
LAICPMS - uncon			0.49	0.999	3.31
LAICPMS - con	1128	130	1.5	0.016	
<i>HA09A2 S3</i>					
SHRIMP - uncon			5.5	0	4.03
SHRIMP - con	1167	110	6.4	0	
<i>HA09A S2</i>					
LAICPMS - uncon			1.2	0.17	4.76
LAICPMS - con	1143	110	1.2	0.18	
<i>HA09A S15</i>					
LAICPMS - uncon			0.56	0.98	5.33
LAICPMS - con	1120	69	0.57	0.98	
<b>TYPE 3</b>					
<i>HA07B S1</i>					
LAICPMS - uncon	no solution				
LAICPMS - con	1064	63	0.55	0.99	
<i>HA07B S9</i>					
LAICPMS - uncon			0.57	0.81	6.4
LAICPMS - con	935	190	0.54	0.85	
<i>HA08A S1</i>					
LAICPMS - uncon			2.2	0.001	6.31
LAICPMS - con	947	110	2.1	0.002	
<i>HA12A S1</i>					
LAICPMS - uncon			1.03	0.42	5.86
LAICPMS - con	1016	44	1.03	0.41	

HA18

SHRIMP - uncon			4	0	4.3
SHRIMP - con	1220	370	4.1	0	
LAICPMS - uncon			1.3	0.14	5.38
LAICPMS - con	1101	38	1.3	0.13	

HA10D

LAICPMS - uncon			0.71	0.96	5.7
LAICPMS - con	1043	28	0.72	0.96	

**TYPE 4**

HA13 S1

LAICPMS - uncon			0.37	1	5.24
LAICPMS - con	1127	27	0.39	1	

HA13 S2

SHRIMP - uncon			4.5	0	5.53
SHRIMP - con	1124	75	5.8	0	
LAICPMS - uncon			0.74	0.94	5.23
LAICPMS - con	1128	23	0.78	0.9	

**ALL**

SHRIMP - uncon	no solution
SHRIMP - con	no solution
LAICPMS - uncon	no solution
LAICMPS - con	no solution

<sup>1</sup>Regressed Tera-Wasserburg plane intercept value. For grains formed between ~1200 and 1000 Ma, concordia (ratio of 207/204 and 206/204 values) intercept value.

<sup>2</sup>Regressed common Pb plane intercept value. For grains formed between ~1200 and 1000 Ma, concordia (ratio of 207/204 and 206/204 values) intercept value.

<sup>3</sup>Ratio of regressed mean 207/204 and 206/204 values giving the upper intercept 207/206 value. Errors on 206/204 values are included.

<sup>4</sup>Unconstrained 3D isochron solution with no restriction on initial Pb composition.

<sup>5</sup>3D isochron regression constrained with initial Pb composition based on the Broken Hills feldspar standard. Broken Hills feldspar standard does not return a solution. Ratios less than zero are not allowed.

<sup>6</sup>3D isochron solution constrained with initial Pb composition based on present day Stacey and Kramers (1975) Pb composition.

odness-of-fit metrics.

	TW plane intercept 207/206 <sup>1</sup>	2σ ±	Common Pb plane intercept 206/204 <sup>2</sup>	2σ ±	Common Pb plane intercept 207/204 <sup>2</sup>	2σ ±
1.4	0.128	0.025	9	27	8.7	4.4
			0	45	12.8	6.2
0.95	0.06	0.12	-4	42	27	27
			0	39	23.3	5.2
0.53	0.089	0.0081	-35	51	5.6	5.8
			0	49	13.5	6.3
0.25	0.0807	0.0084	-8	37	21.5	7.3
			0	37	25.3	4.5
1.6	0.097	0.016	-53	170	9	18
			0	160	13	21
0.73	0.096	0.015	-448	270	-32	29
			0	100	26	12
0.46	0.0888	0.0045	-14	54	6.3	5.4
			0	56	13.3	6.8
0.56	0.078	0.012	-75	110	18	14
			0	90	24	11
0.36	0.0811	0.008	56	54	26.1	7.9
			48	54	28.7	6.4
			100	87	37.1	9.9
1.3	0.078	0.028	280	210	28	35
			280	220	56	23
0.8	0.079	0.033	127	68	33	20
			128	68	38	7.5
0.27	0.081	0.013	75	30	26.9	9.6
			75	30	32	3.8

1.6	0.094	0.022	-42	140	6	16
			0	110	14	15
0.2	0.087	0.016	51	23	27	10
			50	23	33.7	3.8
0.17	0.0765	0.004	143	50	37.2	8.6
			141	51	41.1	5.9
0.14	0.0832	0.0084	36	11	25.5	3.9
			36	11	28	1.9
0.36	0.0844	0.0045	28	19	14.1	2.3
			14	23	15.1	2.8
0.11	0.0838	0.0067	46	11	27.5	3.9
			46	11	30.9	2

---

radiogenic) values are in the range of 5-6.

enetic) values are in the range 0.07-0.08.

4 and 207/204 propagated in quadrature to determine uncertainty on 207/206.

en Hills fsp Pb ratios are: 6/4 = 16.0, 7/4 = 15.39, 8/4 = 35.66, thus 7/6 = 0.962. Used only when a present day Stage

values: 6/4 = 18.5 and 7/4 = 15.6, thus 7/6 = 0.843. Ratios less than zero are not allowed



Common Pb	
plane	
intercept	
$207/206^3$	$2\sigma \pm$

0.967	2.94
undef	undef
-6.750	71.20
undef	undef

-0.160	0.29
undef	undef
-2.688	12.46
undef	undef

-0.170	0.64
undef	undef
0.071	0.08
undef	undef

-0.450	1.78
undef	undef

-0.240	0.40
undef	undef

0.466	0.47
0.598	0.69

0.371	0.34
-------	------

0.100	0.15
0.200	0.18

0.260	0.21
0.297	0.17

0.359	0.19
0.427	0.18

-0.143	0.61
undef	undef
0.529	0.31
0.674	0.32

0.260	0.11
0.291	0.11

0.708	0.24
0.778	0.24

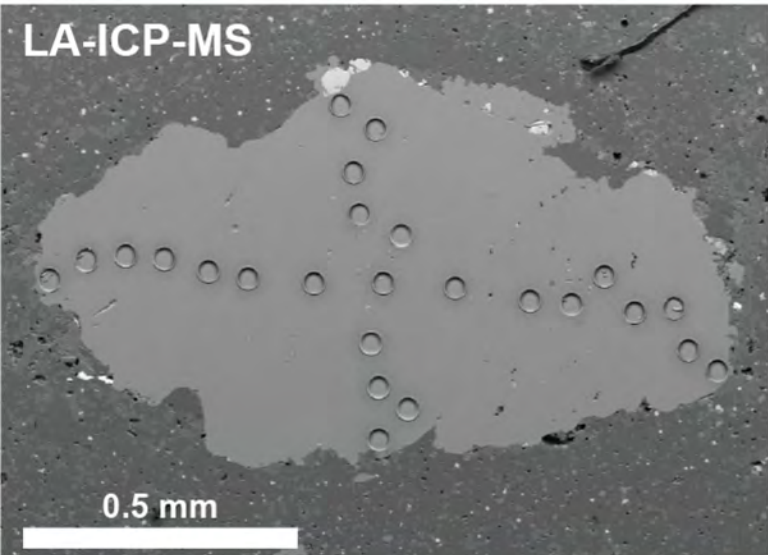
0.504	0.35
1.079	1.78
0.598	0.17
0.672	0.17

---

---

y and Kramers (1975) correction

LA-ICP-MS



SIMS

